Proceedings of the 20th International Conference on Soil Mechanics and Geotechnical Engineering– Rahman and Jaksa (Eds)

Numerical modelling of slope stability for tailing materials with strain-softening and strength anisotropy

Modélisation numérique de la stabilité des pentes pour les stériles miniers présentant un radoucissement et une anisotropie de résistance.

Raffaele Ragni, Hans Petter Jostad & Hongjie Zhou
Norwegian Geotechnical Institute, Australia. raffaele.ragni@ngi.no

Hans Petter Jostad
Norwegian Geotechnical Institute, Norway

ABSTRACT: In this paper, a practical numerical modelling approach is described to assess the stability of slopes / tailing dams. NGI-ADPSoft constitutive model is used, which can capture strain-softening and stress-path dependent strength anisotropy, while being mesh-independent. The capabilities of the model are highlighted through the analysis of a slope stability problem affected by the slow raise of phreatic surface. It is shown that the level of the phreatic surface at which failure occurs is strongly influenced by the properties of the soft material, namely, its undrained shear strength, strength anisotropy and brittleness. Finally, the mesh-independency is demonstrated by obtaining the same failure condition with different mesh coarseness. This is particularly relevant for problems involving softening, where strains would otherwise localise according to the element size, type and orientation, (and thus the thinner the shear zone, the lower the capacity).

RÉSUMÉ: Dans cet article, une approche pratique de modélisation numérique est décrite pour évaluer la stabilité des pentes / barrage stériles de miniers. Nous avons utilisé le modèle constitutif NGI-ADPSoft, qui peut saisir le radoucissement et l'anisotropie de résistance indépendamment du chemin de contraintes, tout en étant indépendant du maillage. Les capacités du modèle sont mises en évidence par l'analyse d'un problème de stabilité de pente affecté par l'élévation lente de la surface phréatique. Il est démontré que le niveau de la surface phréatique auquel la défaillance se produit est fortement influencé par les propriétés du matériau dégradé, à savoir, sa résistance au cisaillement non drainé, son anisotropie de résistance et sa friabilité. Enfin, l'indépendance du maillage est démontrée par l'obtention de la même condition de rupture avec différentes grosseurs de mailles. Ceci est particulièrement pertinent pour les problèmes impliquant un ramollissement, où les déformations seraient autrement localisées en fonction de la taille, du type et de l'orientation de l'élément (et donc, plus la zone de cisaillement est mince, plus la capacité est faible).

KEYWORDS: tailings, slope stability, softening, ADPSoft, phreatic surface

1 INTRODUCTION

Static liquefaction is one of the major contributors to failure of tailing dams worldwide (Davies et al. 2002, AECOM 2009, Morgenstern et al. 2016). It is usually associated with loose, non-plastic materials that tend to contract in volume upon shearing, hence developing excess pore pressures when there is not sufficient time for dissipation. This leads to partial or complete loss of undrained shear strength; failure can happen quite quickly under undrained conditions and without warnings. Common triggers of static liquefaction are increase in phreatic surface, seismic event, toe erosion, rapid loading, etc. Although triggers are often associated with rapid changes, a slow, drained process such as raise in phreatic surface can also initiate the (undrained) static liquefaction (Eckersley 1990, Gens 2019, Reid & Fourie 2019).

Historically, limit equilibrium (LE) methods have been used to assess the stability of slopes for their ease of implementation, with the method of slices among the most common (Fredlund & Krahn 1977). However, LE methods fall short in the slope stability assessment due to the limitations, such as:

- Rigid perfectly-plastic material constitutive models are typically used in the LE methods. Hence the effect of strain compatibility cannot be captured.
- Almost all the LE methods can only use either peak or residual undrained shear strength (or any value in between), instead of mimicking the entire process of post-peak strength reduction. Consequently, they cannot capture the stress redistribution occurring during a progressive failure.

As a result, finite element (FE) approaches are becoming more popular, as they allow the implementation of more realistic and advanced constitutive models. Many of them incorporated the effect of strain softening. However, typical such FE approaches suffer from strain-softening induced strain localisations, and the solution becomes mesh-dependent - the more refined the mesh the more brittle behaviour, and the less stable the slope becomes.

In this paper, NGI-ADPSoft constitutive model is used to perform numerical slope stability analyses. The model is implemented as a user-defined material model in FE code Plaxis 2D (Bentley 2021). For ease of understanding, the example problem presented in the "Slope Stability Round Robin" (Reid 2020) is used to showcase the capabilities of NGI-ADPSoft model. That is, stress-path dependent undrained shear strength, strain softening, and non-local strain for achieving mesh-independency. These are all important factors relevant to typical slope stability assessments.

2 NGI ADPSOFT

The NGI-ADPSoft (from here onwards called ADPSoft) model is a total-stress-based model developed by NGI, which accounts for undrained shear strength, s_u, anisotropy. It was introduced in a 2D formulation by Andresen & Jostad (2002) as ANISOFT,

and later refined and extended to 3D by Grimstad et al. (2010) as ADPSoft.

According to Bjerrum (1973) framework, 'A', 'D' and 'P' stand for Active, Direct Simple Shear, and Passive, respectively. It is often assumed that s_u^C and s_u^E, that is, triaxial Compression and Extension, approximate s_u^A and s_u^P in plane strain. As illustrated in **Error! Reference source not found.**, the model allows for a hardening part, where the shear stress, τ, increases to a peak (p) value, and a softening part, where τ gradually decreases to a residual (r) value. Plastic shear strains, γ, for A, D, and P stress-strain curves are associated to peak and residual shear stresses. The hardening part of the curve follows the formulation of the general NGI-ADP model (Grimstad et al. 2012), whereas parameters c_1 and c_2 offer control over the shape of the softening part of the curve (D'Ignazio et al. 2017). State variables κ_1 and κ_2 indicate the level of hardening and softening achieved ($0 \leq \kappa_1 \leq 1$ for $0 \leq \gamma \leq \gamma_p$, and $0 \leq \kappa_2 \leq 1$ for $\gamma_p \leq \gamma \leq \gamma_r$). The initial, small strain shear modulus is provided as G_0/s_u^A and the model also allows for the specification of an initial, locked-in shear stress, τ_0, in the 'A' and 'P' curves.

To avoid the issue associated with the mesh dependency of the numerical solution, ADPSoft was enhanced with a 'non-local strain' feature (Brinkgreve 1994), wherein the shear strain increment is calculated as an integrated weighted average plastic shear strain increment in a user-defined area around the current integration point. This means that the permanent strain is determined by the deformation within a specific area instead of being dependent on the element size. Briefly, the internal length, l_{int}, and the regularisation parameter, α, give control over the thickness of the shear band, t_{sb}, according to the following equation:

$$t_{sb}/l_{int} = \pi/\sqrt{(\ln(\alpha) - \ln(\alpha - 1))} \quad (1)$$

For an exhaustive description of the non-local strain feature, please refer to Brinkgreve (1994).

For practicality, the model can be calibrated by means of routine laboratory tests, including TXC, TXE, and DSS, without the requirement for more advanced testing (noting, however, that in several cases it is difficult to reach the residual strength in standard tests and the curves need to be extrapolated based either on engineering judgements or model testing. For sensitive clays the residual strength can be reached at several 100% strains). Bender element or similar may be required to measure G_0, although this parameter does not affect the stability greatly and could be safely assumed from values available in literature review or fitted from triaxial curves. For softening problems, this value is also used as unloading modulus, and therefore often called G_{ur}.

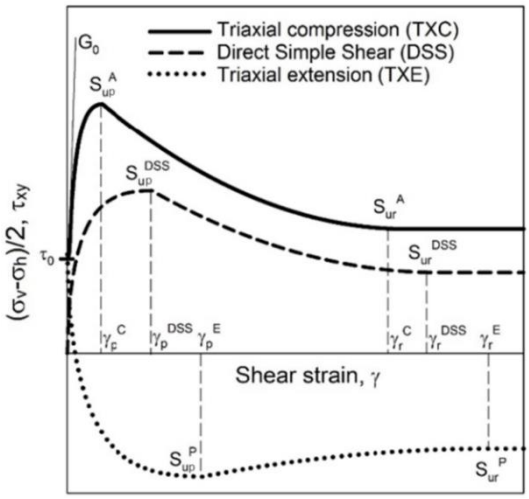

Figure 1. Stress-strain curves of ADPSoft and definition of parameters

3 PROBLEM DEFINITION AND MODELLING DETAILS

The problem presented in the UWA round robin on slope stability (Reid 2020) is used here for illustration. The geometry and initial configuration of the slope is shown in **Error! Reference source not found.**, with the co-ordinates of the key points being listed in **Error! Reference source not found.**. In Reid (2020) round robin, the contestants were asked to provide the phreatic surface level (p.s.l.) at which the slope became unstable. It should be noted that the p.s.l. increases along the vertical line AC with x = 0 m, whereas point H is fixed at all times. Point B in **Error! Reference source not found.** corresponds to y = 25 m.

Table 1. xy coordinates of the slope geometry (after Reid, 2020)

Point (-)	x (m)	y (m)
A	0	0
B	0	25 (Ref)
C	0	50
D	100	0
E	175	25
F	185	25
G	260	0
H	230	0

The plane strain model is composed of ~2250, 15-noded elements in Plaxis 2D (Bentley 2021). The soft material below the phreatic surface is assumed to show a contractive behaviour and is modelled with ADPSoft constitutive model (relevant parameters provided in **Error! Reference source not found.**). Constant values were assumed for the parameters not appearing in **Error! Reference source not found.** ($G_0/s_u^A = 200$, $\tau_0 = 0$, $c_1 = 2$, $c_2 = 2$, $\alpha = 2$, $\nu_u = 0.495$, and a unit weight, $\gamma = 20.3$ kN/m^3). The material above the phreatic surface is assumed non-saturated and showing a fully drained, frictional response ($c' = 1$ kPa, $\phi' = 36^o$, $\psi = 5^o$, and unit weight $\gamma = 18$ kN/m^3).

The undrained strength, s_u, of the saturated, contractive material is expressed as a function of the vertical effective stress, σ'_v. In the reference case, a ratio of $s_u/\sigma'_v = 0.2$ is assumed, derived by adopting an interpreted state parameter from the provided cone resistance profile and Norsand parameters in Reid (2020). Note that a variation in p.s.l. could affect the overconsolidation ratio (OCR) of the soft material. In turn, this may also affect strength and s_u/σ'_v; however, it is hard to quantify the complex interactions among these variables. Moreover, this is believed to be of secondary importance for the purpose of evaluating the stability of the slope. Hence, the effect of a varying OCR on the slope stability was not studied, but instead, a fixed value of s_u/σ'_v was adopted.

Regardless of its actual accuracy, $s_u/\sigma'_v = 0.2$ served as a reference value of the parametric study. A separate, preliminary analysis was thus required to determine σ'_v distribution within the soil domain (to simplify things, a Mohr-Coulomb constitutive model was adopted everywhere, whereas soil weight was as per values provided above). This led to the assumption of an isotropic, average s_u (that is, $s_u^A = s_u^{DSS} = s_u^P$) with distribution shown in **Error! Reference source not found.** for the reference case (Case 0, **Error! Reference source not found.**).

All the analyses featuring in **Error! Reference source not found.** (Case 0 to Case 6) involved two phases for any given p.s.l.: firstly, a state of equilibrium was reached under soil self-weight (using 'Gravity Loading' calculation type in Plaxis 2D); secondly, a small perturbation was introduced in the form of a 2% increase in gravity loading. This was applied to try and trigger a progressive failure, since the problem does not offer in itself an explicit trigger (in the form of, e.g., a foundation load or a seismic action). An increased p.s.l. creates more onerous conditions for the stability; hence, it was increased in increments of 1 m along the Y axis (point B), until the system became

unstable (i.e., a stress equilibrium could not be achieved) under the 2% increase in gravity loading, at which point the p.s.l. at failure was recorded (see **Error! Reference source not found.**).

Two assumptions are made here:

1) The ADPSoft stress-strain curves are only representative of one drainage condition, namely, undrained. However, in this case the stress build-up calculated in the initial phase is considered to occur in drained conditions, even though they are based on stress-strain curves which would be calibrated on undrained tests. Nonetheless, comparison of stress distribution from the preliminary analysis with MC model and the first phase of analyses from **Error! Reference source not found.** showed negligible difference for a given p.s.l.
2) As well recognised, liquefaction caused for example by a slow, drained raising of the p.s.l, is extremely hard to reproduce numerically. In the case of the Norsand model, softening of the internal cap has to be introduced in order to capture this type of failure (Jefferies & Been 2019). However, as mentioned earlier on, the modelling results with Norsand suffer from mesh-dependency due to forming of the shear band. On the other hand, ADPSoft can describe a progressive failure due to the softening part incorporated in its stress-strain curves while being free from mesh dependency, but still requires an 'event' to initiate the failure. In this instance, a 2% increase in gravity loading is sufficiently small for the problem to be still considered realistic, while at the same time large enough to initiate failure. Finally, the consequent increase in frictional capacity of the material above p.s.l. is considered to have minor effect on the global stability of the system.

4 RESULTS

4.1 *Reference case (Case 0)*

The reference case with isotropic $s_u/\sigma'_v = 0.2$ failed when the p.s.l. reached 24 m. **Error! Reference source not found.** shows the maximum shear strain distribution, $(\varepsilon_1 - \varepsilon_2)/2$, at failure. The failure originates near the toe (point H), where σ'_v is at its lowest, develops along the bottom of the tailings domain for ~75 m and then develops upwards with an inclination of ~18º from the horizontal, before it continues into the material above the p.s.l., where the shear band orientation is ~48 º from the horizontal.

By plotting the maximum principal stress directions from the vertical axis (angle θ, Figure 4), it is possible to see the distribution of 'A', 'D' and 'P' zones. The driving, active force at the back is associated with $\theta \sim 0º$, whereas the stabilizing forces from DSS and passive areas are associated with $\theta \sim 45º$ and $\theta \sim 90º$, respectively (keeping in mind, however, the assumption of strength isotropy).

The volume involved in the failure mode downslope can be seen in **Error! Reference source not found.**, which is encompassed by the shear band as defined in **Error! Reference source not found.**.

Error! Reference source not found. shows ADPSoft state variable κ_2, which is an indicator of the degree of softening occurred ($0 \leq \kappa_2 \leq 1$). The area of soft material near the toe has $\kappa_2 = 1$, that is, shear strength has reached the fully residual value. Due to the progressive nature of the failure, gravity will first reach a peak before it starts to reduce and adjacent elements along the shear band start to experience softening ($0 < \kappa_2 < 1$). Note that as the analysis is pushed forward, gravity keeps on reducing, and more elements reach $\kappa_2 = 1$ along the shear band, whilst displacements of the material above the shear band increase. Notice how the material outside of the shear band is not experiencing any degree of softening, i.e., $\kappa_2 \sim 0$.

4.2 *Strength variations (Case 1 and 2)*

In Case 1, both peak and residual undrained strength ratios of the material below p.s.l. were increased by a factor of 1.25 – $s_{u,p}/\sigma'_v$ from 0.2 to 0.25 and $s_{u,r}/\sigma'_v$ from 0.02 to 0.025. This gave a significantly higher p.s.l. at failure, namely, 38 m. The failure mechanism was similar to Case 0 in terms of maximum shear strain distribution.

In Case 2, strength anisotropy was introduced in the form of $s_u^{DSS}/s_u^A = 0.8$ and $s_u^P/s_u^A = 0.6$, with $s_u^{DSS}{}_p/\sigma'_v = 0.2$, while at the same time maintaining the same average su. In other words, same s_u^{DSS}, higher s_u^A and lower s_u^P when compared to Case 0.

The failure mechanism was similar to that observed for Case 0 (Figure 3 to Figure 6), with the shear band developing along the bottom of the tailings domain before propagating into the frictional material above. Failure was achieved at a higher p.s.l. than the reference case (which failed at 24 m), namely, 28 m. This can be explained by considering two factors: (i) the effect of an increased s_u^A on the active side of the failure zone, and (ii) the fact that most of the passive contribution comes from the frictional material above the phreatic surface, thus rendering the reduction in s_u^P inconsequential.

4.3 *Brittleness (Case 3 and 4)*

In Case 3, both γ_p and γ_r were increased two-fold, γ_p from 1 to 2% and γ_r from 30 to 60% (please note that the same values were applied to A, D and P stress-strain curves). This had the effect of creating a more ductile material, with (i) a delayed peak shear strength, and (ii) a less brittle post-peak behaviour. This translates to a slower propagation of the progressive failure, as the soil can offer more resistance in the softening (post-peak) branch for a given strain level when γ_r is increased. Likewise, the soil develops less shear stress, τ, for the same imposed strain in the hardening (pre-peak) branch. As a result, Case 3 reached failure at a p.s.l. of 26 m. The failure mechanism developed along the bottom of the tailings domain for a longer distance than Case 0 (~85 m) before deviating upwards.

In Case 4, brittleness of the soft material below p.s.l. was increased by lowering γ_p to 0.51% and γ_r to 10% (note that γ_p must be larger than the elastic strain, $\gamma_e = 0.5\%$). As expected, failure occurred at a lower p.s.l. (22 m). The failure mechanism deviated slightly from what observed in Case 0; from point H (**Error! Reference source not found.**), it developed along the bottom for ~45 m, before deviating at upwards at 17º angle to join the boundary between the two materials. It then developed along the boundary for further ~35 m, with the shear band trying to follow the zone with lowest s_u. Finally, it deviated again into the frictional material at an angle of 51º. This last deviation occurred roughly at (x; y) = (127.5 m; 9.8 m), thus resulting in less overall material displaced when compared to Case 0.

It should be mentioned that a more detailed application of γ_p and γ_r, that is, different stain levels for A, D and P stress-strain curves would produce more accurate results. However, at this stage the example reported is considered to illustrate sufficiently accurately the effect of these two parameters on the overall slope stability.

4.4 *Shear band thickness (Case 5 and 6)*

The effects of the shear band thickness, t_{sb}, on the slope stability discussed in this section are of qualitative nature. The exact definition of t_{sb} is *per se* a very complex problem in undrained condition, which has not been attempted here. Jostad & Andresen (2006), Thakur (2007) and Gylland et al. (2013) studied the problem in the past, but the problem is still not fully understood, as it involves a complex interaction of local pore water flow and deformation rate (differently from granular material, where t_{sb} depends on the average grain size).

Case 5 and Case 6 aimed to show (i) the effect of the shear band thickness, t_{sb} (which can be controlled with ADPSoft via the parameter l_{int}), on the overall stability, and (ii) the mesh-independence of the model, provided the same t_{sb} is adopted (see Eq. 1).

Case 5 looked at increasing the parameter l_{int} from 1 to 2 m, effectively doubling t_{sb}. It is acknowledged that a thicker shear band gives less brittle behaviour (similarly to increased γ_r), since for a given displacement, u, of the soil mass above the shear band, the shear strain within the shear band, $\gamma = u/t_{sb}$, becomes smaller and the reduction in shear strength is mitigated. Although quite small for this case, it reflected in a p.s.l. at failure that increased from 24 m (Case 0) to 25 m.

Both Case 0 and Case 5 adopted a mesh with average element size along the shear band of ~ 1 m (see **Error! Reference source not found.** top). This average size was deliberately increased to ~ 2 m in Case 6 (**Error! Reference source not found.** bottom), whilst $l_{int} = 2$ m was confirmed. The shear band thickness without regularisation depends on element type (interpolation functions) and orientation. For a 6-node triangular element, the shear band thickness varies between ½ and 3 times the element size, while for 15-node triangular element between ⅓ and 1 time the element size, depending on the orientation of the element compared to the shear band (both element types are available in Plaxis 2D).

Case 6 failed at the same p.s.l. of Case 5, i.e., 25 m, showing the ability of the model to provide a solution which is independent of the mesh coarseness adopted. Normally, the shear band would collapse to the size of a single element, causing Case 5 to provide a more onerous (i.e., lower p.s.l.) case. However, in this case control of the shear band thickness t_{sb} is not governed by the mesh but is imposed via the parameter l_{int}.

5 SUMMARY AND CONCLUSIONS

The numerical study presented in this paper offers an efficient and robust solution to the problem of slope stability with slow raise of phreatic surface level (p.s.l.), which can lead to static liquefaction when soft material is present. Although the pore pressure distribution is ignored (the analyses are in total stresses), the constitutive model NGI-ADPSoft does model the post-peak strength reduction caused by this shear-induced pore pressure, making it a suitable candidate for the modelling of progressive failures. Furthermore, it is calibrated by means of routine laboratory tests, such as monotonic undrained triaxial compression and extension, TXC and TXE, and direct simple shear, DSS, without the requirement for more advanced testing.

The analyses highlighted the capabilities of the NGI-ADPSoft constitutive model to numerically capture the progressive failure occurring in a slope stability problem of a soft material such as tailing. In addition to the strain-softening effect, stress-path dependent strength anisotropy can also be accounted for by this model in a practical manner.

Results show that the undrained shear strength, which is affected by the level of the p.s.l., has a large influence on the slope stability. A relatively modest increase in normalised strength, s_u/σ'_v from 0.2 to 0.25 allowed the p.s.l. to raise a further 14 m before failure was reached. Hence, care should be applied when determining the strength of the soil below the phreatic surface. Likewise, the variation of material brittleness (in the form of different strains at peak and residual strength) allowed for a different p.s.l. at failure. As expected, a more brittle material led to failure at lower p.s.l., and vice versa.

The introduction of strength anisotropy factors, that is, $s_u^A > s_u^{DSS} > s_u^P$ (as opposed to $s_u = s_u^{DSS}$ everywhere) whilst maintaining the same average s_u, also led to an increase of the p.s.l. at failure. This was, however, dependent on the geometry of the problem and the arbitrary values assumed for demonstrative purposes. Different anisotropy ratios or geometry of the active, passive and DSS zones can lead to different outcomes, e.g., a lower capacity.

Finally, the ability of the model to actively control the shear band thickness, and its effect on the overall slope stability were demonstrated. It was shown that (i) a larger shear band thickness leads to a more stable slope, albeit with a limited effect for the considered problem, and (ii) the use of the non-local strain feature (via the parameter l_{int}) renders the problem mesh-independent. It should be mentioned that the paper only aimed to show a qualitative study of shear band thickness, t_{sb}, without trying to quantify its exact value, as this is *per se* a very complex problem in undrained condition (Jostad & Andresen 2006, Thakur 2007, Gylland et al. 2013).

6 REFERENCES

AECOM 2009. Root cause analysis of TVA Kingston dredge pond failure on December 22, 2008. Vernon Hills, IL, USA.

Andresen L. and Jostad H.P. 2002. A constitutive model for anisotropic and strain-softening clay. *Proc. of the Numerical Models in Geomechanics*, 581-585.

Bentley 2021. Plaxis 2D Reference Manual.

Bjerrum L. 1973. Problems of Soil Mechanics and Construction on Soft Clays. State of the Art Report to Session IV. *Proc. 8th International Conference on Soil Mechanics and Foundation Engineering*, Moscow, 111-159.

Brinkgreve R.B.J. 1994. Geomaterial models and numerical analysis of softening, *PhD thesis*, TU Delft, The Netherlands.

Davies M.P., Mcroberts E.C. and Martin T.E. 2002. Static liquefaction of tailings – fundamentals and case histories. Proceedings of Tailings Dam 2002: *Proc. of the Joint ASDSO/USSD Specialty Conference*, Las Vegas, NV, USA, 233–255.

D'Ignazio M., Länsivaara T.T. and Jostad H.P. 2017. Failure in anisotropic sensitive clays: finite element study of Perniö failure test. *Canadian Geotechnical Journal*, 54(7), 1013-1033.

Eckersley D. 1990. Instrumented laboratory flowslides. *Geotechnique*, 40(3), 489-502.

Fredlund D.G. and Krahn J. 1977. Comparison of slope stability methods of analysis. *Canadian geotechnical journal*, 14(3), 429-439.

Gens Solé A. 2019. Hydraulic fills with special focus on liquefaction. *Proc. of the XVII ECSMGE-2019: Geotechnical Engineering foundation of the future*, 1-31.

Grimstad G., Jostad H.P. and Andresen L. 2010. Undrained capacity analyses of sensitive clays using the nonlocal strain approach. *Proc. of the 9th HSTAM International Congress on Mechanics,* Limassol, Kypros, 12–14 July, 153–160.

Grimstad G., Andresen L. and Jostad H.P. 2012. NGI-ADP: Anisotropic shear strength model for clay. *International journal for numerical and analytical methods in geomechanics*, 36(4), 483-497.

Gylland A.S., Rueslåtten H., Jostad H.P. and Nordal S. 2013. Microstructural observations of shear zones in sensitive clay. *Engineering Geology*, 163, 75-88.

Jefferies M. and Been K. 2019. Soil liquefaction: a critical state approach. *CRC press*.

Jostad H.P., Andresen L. and Thakur V. 2006. Calculation of shear band thickness in sensitive clays. *Proc. 6th European Conference on Numerical Methods in Geotechnical Engineering*, Graz, Austria, 27-32.

Morgenstern N.R., Vick S.G., Viotti C.B. and Watts B.D. 2016. Fundão tailings dam review panel: report in the immediate causes of the failure of the Fundão Dam.

Reid D. and Fourie A. 2019. A direct simple shear device for static liquefaction triggering under constant shear drained loading. *Géotechnique Letters*, 9(2), 142-146.

Thakur V. 2007. Strain localization in sensitive soft clays. *PhD Thesis*, NTNU, Trondheim, Norway.

Reid 2020. Slope Stability Round Robin. The University of Western Australia, Perth, Australia.

Table 2. Summary of ADPSoft parameters object of the parametric study

Case	$s_u^{DSS}{}_{,p}/\sigma'_v$	$s_u^{DSS}{}_{,r}/\sigma'_v$	s_u^{DSS}/s_u^{A*}	s_u^{P}/s_u^{A*}	γ_p	γ_r	Ave. elem. Size**	l_{int}	P.s.l. at failure
(-)	(-)	(-)	(-)	(-)	(%)	(%)	(m)	(m)	(m)
0	0.2	0.02	1	1	1	30	1	1	24
1	*0.25*	*0.025*	1	1	1	30	1	1	38
2	0.2	0.02	*0.8*	*0.6*	1	30	1	1	28
3	0.2	0.02	1	1	*2*	*60*	1	1	26
4	0.2	0.02	1	1	*0.51*	*10*	1	1	22
5	0.2	0.02	1	1	1	30	1	*2*	25
6	0.2	0.02	1	1	1	30	*2*	*2*	25

Values in *italics* represent deviation from reference case (Case 0)
* Anisotropy factors only applied to peak strength
** Approximate value along the shear band

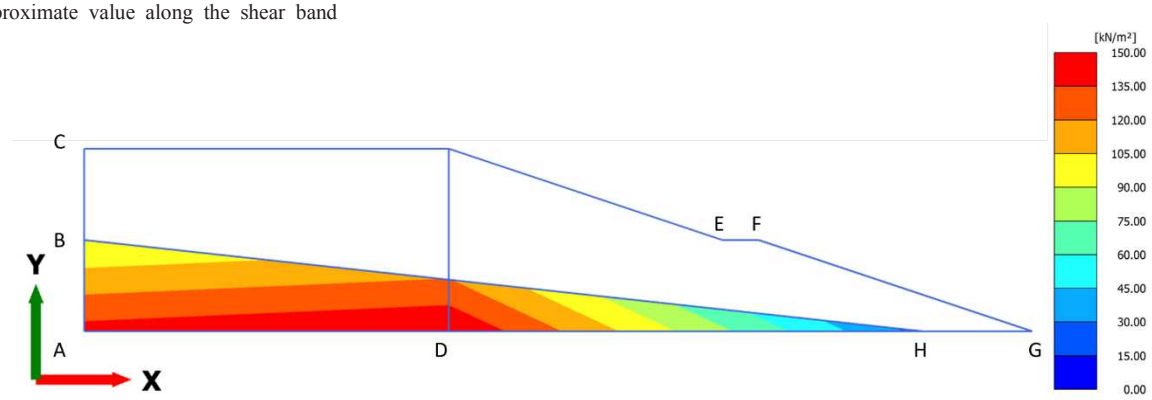

Figure 2. Geometry of the problem and s_u distribution for reference case

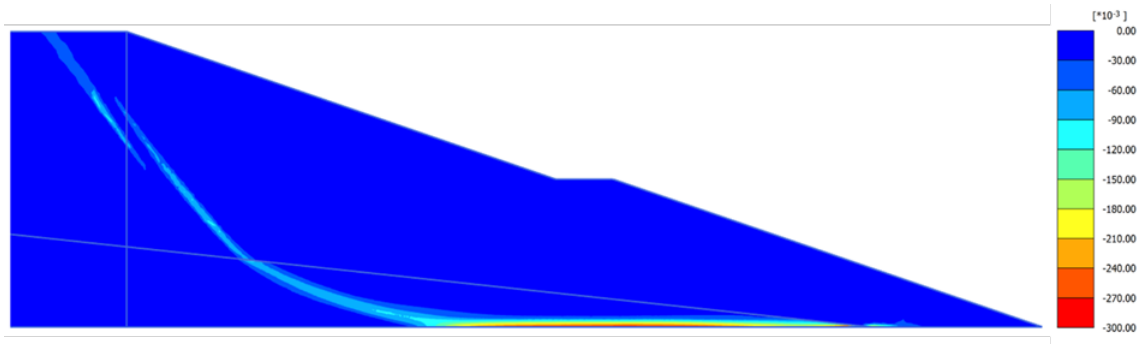

Figure 3. Maximum shear strains $(\varepsilon_1 - \varepsilon_3)/2$ for Case 0 with p.s.l. at 24 m

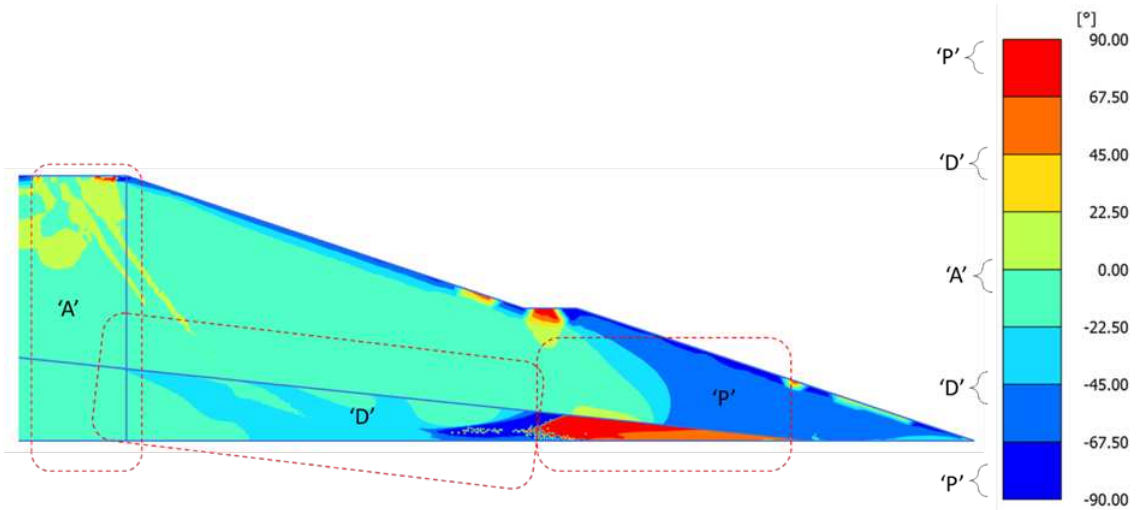

Figure 4. Maximum principal stress directions from the vertical axis, θ, for Case 0 with p.s.l. at 24 m – 'A': θ = 0º, 'D': θ = 45º, 'P': θ = ±90º (enveloped areas are indicative only)

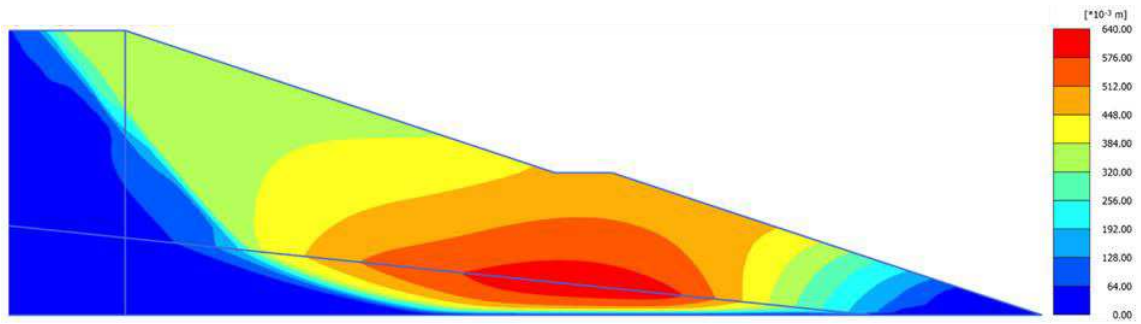

Figure 5. Total displacement magitude |u| for Case 0 with p.s.l. at 24 m

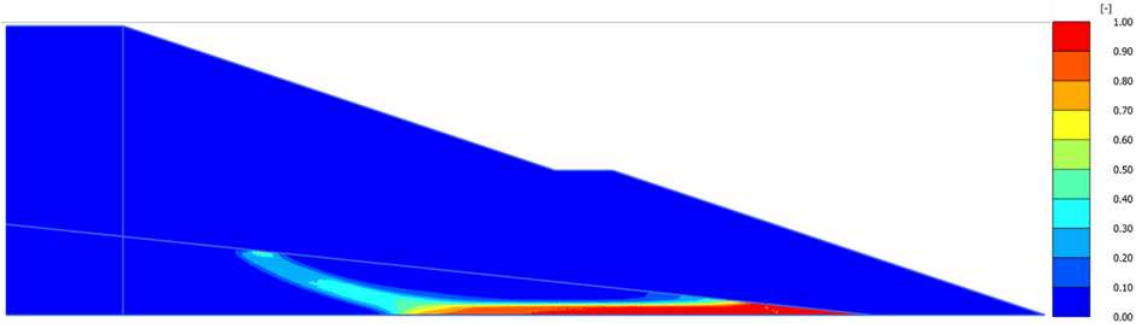

Figure 6. ADPSoft parameter κ_2 for Case 0 with p.s.l. at 24 m

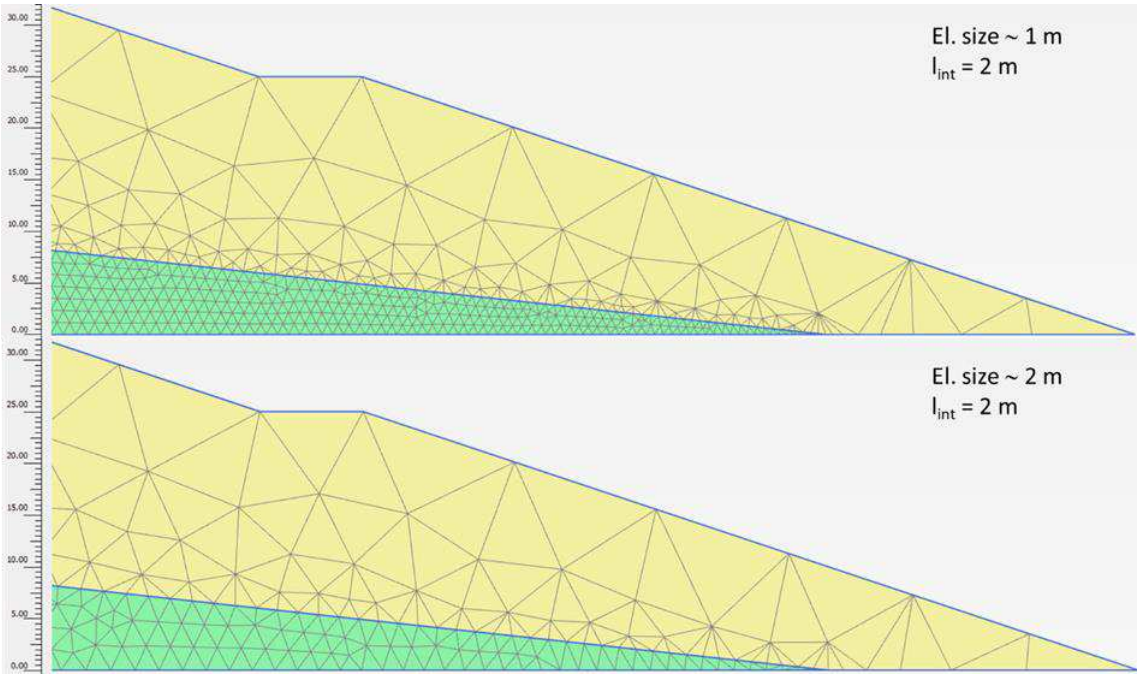

Figure 7. Comparison of mesh coarseness between Case 5 (top) and Case 6 (bottom)